Numerical study of shock/boundary layer interaction in supersonic overexpanded nozzles

A. Hadjadj [a,*], Y. Perrot [a], S. Verma [b]

[a] *National Institute of Applied Sciences, INSA & CORIA – UMR 6614 C.N.R.S., Avenue de l'Université BP8, 76801 Saint Etienne du Rouvray, France*
[b] *National Aerospace Laboratories (CSIR), Bangalore, India*

A B S T R A C T

A numerical study, using a mixed finite element/finite volume method on unstructured meshes adapted for compressible flows, is conducted to investigate turbulent boundary-layer separation in overexpanded subscale supersonic nozzles including shock/shock and shock/boundary layer interactions. Two test-cases are investigated, namely a TIC (Truncated Ideal Contour) nozzle and a TOP (Thrust Optimized Parabolic contour) nozzle with a secondary jet injection. Particular attention is paid to the appearance of a recirculation region downstream of the Mach disc as well as in the vicinity of the secondary nozzle exit. The results so obtained are analyzed and compared with the experimental data. The results suggest that very different shock structures and flow separation may appear depending on the nozzle contour as well as on the operating pressure and temperature ratios. In the case of TOP nozzle, the simulations reveal the existence of a small recirculation bubble at the vicinity of the secondary injection, due to a shock/boundary layer interaction. In addition, it has been shown that, at high temperature ratios, compressibility effects on the growth rate of the mixing layer, which develops between the main stream and the secondary jet injection, become significant and cannot be neglected in the computation.

© 2015 Elsevier Masson SAS. All rights reserved.

1. Introduction

Flow separation control in rocket nozzles is a challenging problem in aerospace science, not only for current engines confronted with problems of thermo-mechanical resistance, but also for future engines which could work with very wide separation zones. This problem is particularly important for aerospace applications (rockets and missiles).

Flow separation in supersonic nozzles is a basic fluid-dynamics phenomenon that occurs at a certain range of pressure ratios, resulting in shock formation and shock/turbulent-boundary layer interaction inside the nozzle. Basically, the physical problem encountered in nozzle flows is essentially the result of boundary-layer separation caused by an adverse pressure gradient (see Fig. 1) which interacts with shocks and gives rise to complex phenomena. This problem involves basic structure of shock interactions with separation shock, which consists of incident shock, direct or inverse Mach reflections, reflected shock, triple point and slip lines. Several complex purely viscous phenomena, such as boundary layers with adverse pressure gradients, induced separation, recircula-

tion bubbles, shear layers can occur in nozzles and may strongly affect the engine's performance. In addition, from a purely gas-dynamics point of view, the heat loading in propulsive nozzles can be considerable, since most of these phenomena occur in hot gases at very high temperature with complex chemical reactions and important heat-transfer mechanisms.

Previous studies on supersonic nozzles [21,44,45] have shown that shock-wave/boundary layer interaction (SWBLI) occurring in highly overexpanded nozzles may exhibit strong unsteadiness that cause unsymmetrical flow separation. In the rocket design community, shock-induced separation is considered undesirable because the inherent shock unsteadiness and flow asymmetry can cause dangerous lateral forces, the so-called side-loads, which may damage the nozzle [25]. This phenomenon has received significant attention in the past and still is an active subject of research and development, the prime motive of which has been to improve nozzle performance under overexpanded flow conditions and to mitigate side-loads in nozzles during impulsive startup and shut down operation.

Several experimental studies, performed on either subscale [17, 26,27] or full-scale [25] optimized nozzles, corroborated by different numerical simulations [6,7,13], demonstrated the existence of two distinct separation processes, namely the Free Shock Separa-

Nomenclature

c	speed of sound
k	turbulent kinetic energy
L	nozzle length
M_c	convective Mach number
$\mathcal{P}_k$	production of turbulence kinetic energy
p	static pressure
R	radius
S_{ij}	rate of strain tensor
Ω_{ij}	vorticity tensor
T	static temperature
u_i	velocity component in the x_i direction
u_τ	friction velocity
δ_ω	vorticity thickness
ε	turbulent dissipation rate
γ	ratio of specific heats
μ	dynamic viscosity
ω	specific dissipation rate
ρ	density
Θ	temperature ratio

Subscripts

a	ambient condition
c	chamber or reservoir condition
t	turbulent quantity
w	wall value
mf	main flow quantity

Superscripts and overline

$\overline{(\ )}$	Reynolds-averaged quantity
$\widetilde{(\ )}$	density weighted average ($\widetilde{F} = \overline{\rho F}/\overline{\rho}$)
$'$	Reynolds (centred) fluctuation ($f' = F - \overline{F}$)
$''$	Favrian fluctuation ($f'' = F - \widetilde{F}$)

Abbreviations

|	
CFD	computational fluid dynamics
FSS	free shock separation
NPR	nozzle pressure ratio
RSS	restricted shock separation
SWBLI	shock-wave/boundary-layer interaction
TIC	truncated ideal contoured nozzle
TOP	thrust-optimized parabolic nozzle
TVD	total variation diminishing
RANS	Reynolds-Averaged Navier–Stokes
URANS	unsteady RANS
LES	large-eddy simulation
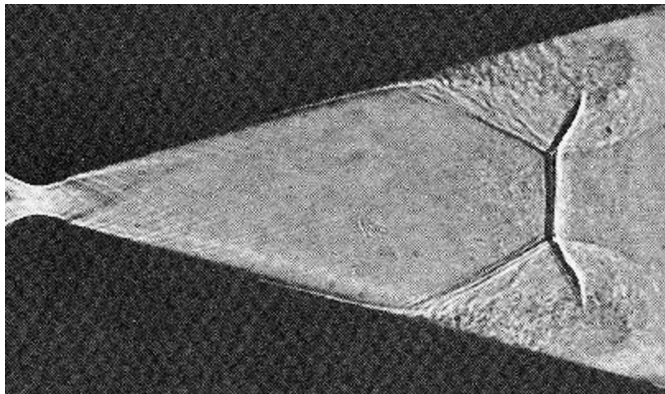
Fig. 1. Shock/boundary layer interaction in a planar supersonic nozzle. Experimental Schlieren photograph [3].

tion (FSS), in which the boundary layer separates from the nozzle wall and never reattaches, and the Restricted Shock Separation (RSS) characterized by a closed recirculation bubble, downstream of the separation point, with reattachment on the wall. These two type of flow separation occur during transient startup or shutdown even if the nozzle operates with full-flow at steady-state chamber pressure. In a typical rocket engine during startup, the chamber pressure rises from the ambient pressure value to the steady state operating value over a short time duration. Flow separation momentarily occurs when the chamber pressure is relatively low, such as to yield wall pressure much lower than the ambient value at some location in the nozzle divergent section. In case of a TOP nozzle during transient startup, the separated flow is first governed by the FSS structure. Then the FSS is replaced by the RSS pattern when the chamber pressure exceeds a certain critical value. Hysteresis of the FSS ↔ RSS transition is also clearly identified and several peaks in side-loads are measured by different groups in Europe [28,39], USA [25] and Japan [40]. In spite of many studies on the subject (see for example the recent thematic issue on nozzle flow separation [16]), the mechanism of flow separation leading to transverse unsteady forces is quite complex, and fundamental knowledge of supersonic flow physics in the presence of shock reflection at wall, shock/shock and shock/boundary layer interactions is still needed.

Today with recent progress in computer science, a significant number of realistic flows with complex phenomena are considered with the help of numerical simulation. Advances in this field need accurate simulations using reliable flow solvers with increasingly significant data-processing resources based on powerful computers. From a computational and modeling point of view, compressible flows, in general, and shock/boundary-layer interaction, in particular, pose substantial challenges. Although some features of this interaction are also encountered in other boundary layers subjected to smoothly varying adverse pressure gradient, there are aspects that make the prediction of shock-affected flows especially difficult. There is, first, the question of numerical accuracy and shock-capturing methods in which the approximation of the numerical fluxes is of considerable importance. Modern low-dissipative high-order methods, based on Riemann solvers and high-order WENO interpolation, are now generally regarded as offering an accurate and stable numerical framework. However, their complexity, especially when applied to general 3D turbulent flows, has encouraged the use of simpler, arguably less adequate approaches, such as Jameson-type artificial viscosity methods, and TVD schemes. As regards turbulence, significant progress has been made in the development of both steady (RANS) or unsteady hybrid (RANS/LES) methods, which incorporate configuration-dependent flow physics. Within the class of RANS methods, two-equation turbulence models have been used most frequently for free supersonic jets and nozzles analyses because of their capability to provide mean flow and turbulent kinetic energy fields necessary for subsequent SWBLI analysis. In this context, there have been several investigations of turbulence models for jet flows originating from a variety of nozzle configurations such as those in Refs. [8,11,18,48]. A comprehensive review of turbulence model development in the PAB3D code (which is a three-dimensional RANS solver with a finite-volume formulation on structured multi-block grids, developed at NASA Langley Research Center) and evaluation for a variety of nozzle flows is pre-

sented by Abdol-Hamid et al. [1]. Also, an assessment of RANS methods for SWBLI problems can be found in the AGARD report edited by Knight and Degrez [19]. While the majority of supersonic nozzle flow simulations to date have been conducted using structured grids, some recent efforts, such as that of Pao et al. [29], have been made on unstructured grids.

In the present paper, we report some progress in the computation of supersonic nozzle flows using an unstructured fully compressible Navier–Stokes code in which the near-wall turbulence modeling approach has been improved. To account for the effects of compressibility, Sarkar's [36,37] corrections were employed. The paper is organized as follows: in the following section, the turbulence model as well as the numerical tool are briefly described. Results are then presented for both TIC and TOP nozzles including a secondary jet injection. Concluding remarks are then given at the end of the paper.

2. Turbulence closure, solver and grid strategy

2.1. Turbulence modeling

Among the two-equation turbulence models widely used, the Shear-Stress Tensor (SST) Menter [22] is one of the most accurate model since it combines advantages of $k-\omega$ near walls and $k-\varepsilon$ in wakes and free-shear flow regions. As suggested by Zeman [49] and Sarkar et al. [36,37] for highly compressible flows, compressibility effects may be included in the two-equation turbulence models to account for the turbulent dissipation reduction through the pressure–dilatation correlation. In this study, we have added the compressibility corrections [15,20,36,37] to the standard version of the SST-Menter turbulence model. Based on the Boussinesq eddy viscosity concept, the $k-\omega$ SST turbulence model uses two transport equations to describe the turbulence as summarized below:

Turbulence energy equation:

$$\underbrace{\frac{D(\rho k)}{Dt}}_{Transport} = \underbrace{\mathcal{P}_k}_{Production} + \underbrace{\frac{\partial}{\partial x_j}\left[(\mu + \sigma_k \mu_t)\frac{\partial k}{\partial x_j}\right]}_{Diffusion}$$

$$\underbrace{- \beta^* \rho \omega k\left[1 + \alpha_1 M_t^2(1 - F_1)\right]}_{Destruction} + \underbrace{(1 - F_1)\overline{p''d''}}_{Pressure-dilatation} \quad (1)$$

where k is the turbulent kinetic energy per unit mass defined as $k = \frac{1}{2}\widetilde{u_i'' u_i''}$, and the two additional terms $\alpha_1 M_t^2 \rho \omega k$ and $\overline{p''d''}$ represent the contributions due to compressible dissipation and pressure dilatation, respectively.

Specific-dissipation rate equation:

$$\frac{D(\rho\omega)}{Dt} = \frac{\gamma}{\nu_t}\mathcal{P}_k + \frac{\partial}{\partial x_j}\left[(\mu + \sigma_\omega \mu_t)\frac{\partial \omega}{\partial x_j}\right]$$

$$- \beta^* \rho \omega^2\left[1 + \alpha_1 M_t^2(1 - F_1)\right] - (1 - F_1)\frac{\overline{p''d''}}{\nu_t}$$

$$+ \underbrace{2\rho(1 - F_1)\sigma_{\omega 2}\frac{1}{\omega}\frac{\partial k}{\partial x_j}\frac{\partial \omega}{\partial x_j}}_{Cross-diffusion\ term} \quad (2)$$

in which the turbulent viscosity is expressed as

$$\mu_t = \frac{a_1 \rho k}{\max[a_1\omega(1 + \alpha_1 M_t^2(1 - F_1)), \Omega F_2]} \quad (3)$$

The left hand side of Eqs. (1) and (2) is the Lagrangian derivative, $D/Dt := \partial/\partial t + u_i \partial/\partial x_i$, and $\mathcal{P}_k = -\bar{\rho}\widetilde{u_i'' u_j''}(\frac{\partial \widetilde{u_i}}{\partial x_j})$ is the exact turbulent kinetic energy production. Here, $-\bar{\rho}\widetilde{u_i'' u_j''}$ are the Reynolds stresses.

Based on direct numerical simulation of turbulent shear flows, Sarkar et al. [37] proposed the following model for pressure dilatation:

$$\overline{p''d''} = -\alpha_2 \mathcal{P}_k M_t^2 + \alpha_3 \bar{\rho}\varepsilon_s M_t^2$$

Here $M_t = \frac{\sqrt{2k}}{c}$ is the turbulent Mach number and c is the local speed of sound.

The model constants are: $\beta^\star = 0.09$, $\sigma_k \in [0.85-1]$, $\sigma_\omega \in [0.5-0.85]$, $a_1 = 0.31$, $\alpha_1 = 0.5$, $\alpha_2 = 0.4$, $\alpha_3 = 0.2$, Ω is the vorticity magnitude, and F_1, F_2 are two blending functions used to ensure smooth transition between $k-\epsilon$ and $k-\omega$ formulations [22].

2.1.1. Improvement of the numerical robustness

Close to the wall, it is necessary to use very fine meshes in order to correctly capture the viscous sublayer. Due to the stiffness of the mean flow gradient, the solver may detect locally non-physical solutions, like negative turbulent values (especially for k). In addition, during transient phases of the computation, turbulent viscosity peaks may appear due to spurious numerical oscillations, which may preclude the convergence of the numerical solution, especially in stagnant regions. To avoid such problems, we have implemented a number of specific treatments of turbulent quantities in order to reinforce the robustness of the numerical code.

2.1.1.1. Vorticity limitation
According to Boussinesq and based on the realizability conditions, the turbulent shear stress should verify the following inequality:

$$\frac{2}{3}\rho k - 2\mu_t\left(S_{ii} - \frac{1}{3}\frac{\partial \widetilde{u_k}}{\partial x_k}\right) \geq 0, \quad i = 1, 2, 3 \quad (4)$$

From (4), we have:

$$\mu_t \leq \frac{1}{3}\frac{\rho k}{\left(S_{ii} - \frac{1}{3}\frac{\partial \widetilde{u_k}}{\partial x_k}\right)}, \quad i = 1, 2, 3 \quad (5)$$

with $S_{ij} = \frac{1}{2}(\frac{\partial \widetilde{u_i}}{\partial x_j} + \frac{\partial \widetilde{u_j}}{\partial x_i})$. Thus:

$$\mu_t \leq \frac{1}{3}\frac{\rho k}{\left(\frac{\partial \widetilde{u_i}}{\partial x_i} - \frac{1}{3}\frac{\partial \widetilde{u_k}}{\partial x_k}\right)}, \quad i = 1, 2, 3 \quad (6)$$

From the definition of the turbulent eddy viscosity and the expression (6), it is possible to obtain the lower limit of ω as:

$$(\rho\omega)_{\min} = \rho\left|\frac{\partial \widetilde{u_i}}{\partial x_i}\right|, \quad i = 1, 2, 3 \quad (7)$$

The expression (7) corresponds to a spatial limitation of the vorticity.

In addition, during the transient phase of the startup computation, the turbulent values can become negative. To avoid such a problem, we have implemented the following treatment [31]:

$$\Delta\rho k = (\rho k)^{n+1} - (\rho k)^n \leq \frac{1}{2}(\rho k)^{n+1}$$

$$\text{hence } (\rho k)^{n+1} \leq 2(\rho k)^n \quad (8)$$

$$\Delta\rho\omega = (\rho\omega)^{n+1} - (\rho\omega)^n \leq \frac{1}{2}(\rho\omega)^{n+1}$$

$$\text{hence } (\rho\omega)^{n+1} \leq 2(\rho\omega)^n \quad (9)$$

where n is the index for the time advancement. Relations (8) and (9) represent a numerical limitation which is particularly useful for unstructured meshes since it automatically limits steep temporal variation of the turbulent values, avoiding thereby any accidental code blowing-up.
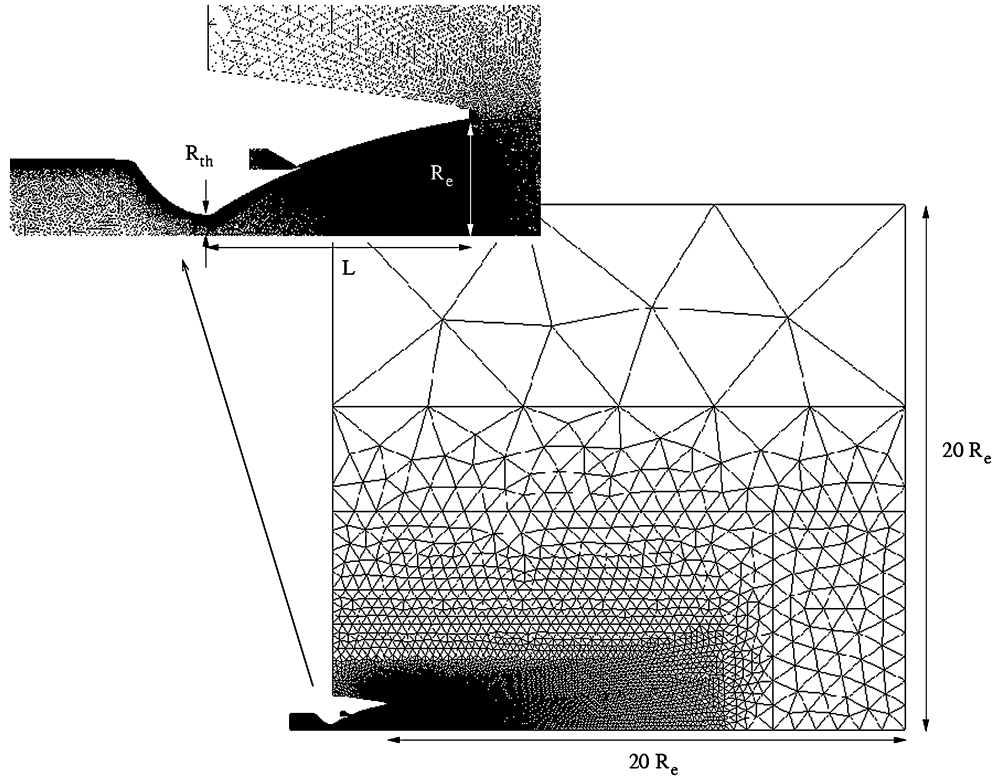
Fig. 2. Example of the TOP nozzle mesh and computational domain with $R_e/R_{th} \simeq 5.65$ and $L/R_{th} = 12.5$ with $R_{th} = 1$ cm.

2.1.1.2. Realizability condition Most of the two-equation eddy viscosity turbulence models are based on the Boussinesq assumption where the Reynolds stresses are expressed as a linear function of the mean strain tensor:

$$-\rho \widetilde{u_i'' u_j''} = 2c_\mu \frac{\rho k^2}{\varepsilon}\left(S_{ij} - \frac{1}{3}S_{ll}\right) - \frac{2}{3}\rho k \delta_{ij} \qquad (10)$$

where $c_\mu = 0.09$. As shown by Moore and Moore [23], these equations can give negative values for the normal stresses if $S_{ll}\frac{k}{\varepsilon}$ is too large. Bradshaw on the other hand, has noticed that in two-dimensional boundary layers submitted to a strong pressure gradient the shear stress was approximately proportional to the turbulent kinetic energy with:

$$-\widetilde{u_1'' u_2''} \approx \sqrt{c_\mu} k \qquad (11)$$

These two remarks led to the introduction of weakly nonlinear turbulence models in which the c_μ factor is allowed to vary dynamically according to:

$$c_\mu = \min\left(0.09, \frac{1}{A_0 + A_S(S^{*2} + A_\Omega \Omega^{*2})^{1/2}}\right) \qquad (12)$$

with

$$\begin{cases} S^* = \dfrac{1}{\omega \beta^*}\sqrt{2S_{ij}S_{ij} - \dfrac{2}{3}S_{kk}^2} \\ \Omega^* = \dfrac{1}{\omega \beta^*}\sqrt{2\Omega_{ij}\Omega_{ij}} \end{cases}$$

where $\Omega_{ij} = \frac{1}{2}(\frac{\partial \widetilde{u_i}}{\partial x_j} - \frac{\partial \widetilde{u_j}}{\partial x_i})$ and $A_0 = 0$, $A_S = 2.10$, $A_\Omega = 1$. This set of constants were chosen as in Gross and Weiland [12].

The use of realizability conditions helps to improve robustness and numerical stability, especially for steady state solutions. This condition has also advantage to limit the turbulent viscosity in regions submitted to large strain rates, like in strong shocks where many models tend to produce high-turbulence levels downstream of a normal shock.

2.2. Solver and numerical methods

Computations are performed using the Computational Fluid Dynamics (CFD) code *N3S-Natur* [38], which is a general-purpose, full unstructured parallel compressible Navier–Stokes solver, developed by the SAFRAN group and its partners. Currently, the N3S-Natur code is being used in France by both researchers and industrial groups for many practical applications (nozzles, turbo-machines, jet propulsion, combustion and many other aerothermodynamics applications). This code uses a mixed finite-volumes (for the convective terms)-finite elements (for diffusive and source terms) method based on unstructured meshes made of multiple elements. The convective fluxes are integrated by a finite volume method with a second-order MUSCL (Monotone Upstream-centered Schemes for Conservation Laws) TVD technique [5,43] based on the Roe solver [35] to capture discontinuities, whereas source and diffusive terms are integrated by a finite element method. The time integration uses a second-order explicit/implicit scheme to advance the solution, with an efficient preconditioned linear solver. Several turbulence models and advanced numerical techniques are also included in this code.

For nozzle computations, an unstructured mesh with triangular cells is used, and grid points are clustered in regions of high gradients (see Fig. 2). For example, to ensure mesh-independent solution, the first grid point is located at $y_1^+ = u_\tau d_w/\nu \simeq 1$ (where u_τ is the friction velocity and d_w the distance to the closet wall). In addition, the mesh is stretched in both axial and radial directions to enable matching the fine grid clustering near the nozzle wall to the coarse grid in the regions far away from it. Also, finer grid clustering is used in the axial direction to capture the birth and the early growth of the shear layer as well as the shock cells structure. Extensive grid refinement tests were achieved to insure that the results (at least the first- and second-order statistics) are
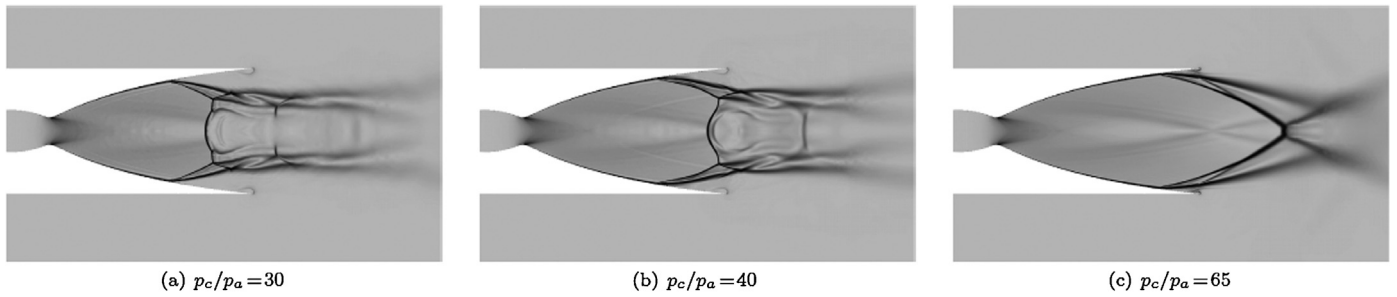
(a) $p_c/p_a = 30$ (b) $p_c/p_a = 40$ (c) $p_c/p_a = 65$

Fig. 3. Numerical Schlieren pictures of the TIC nozzle at three different NPR with $\Theta = 1$.

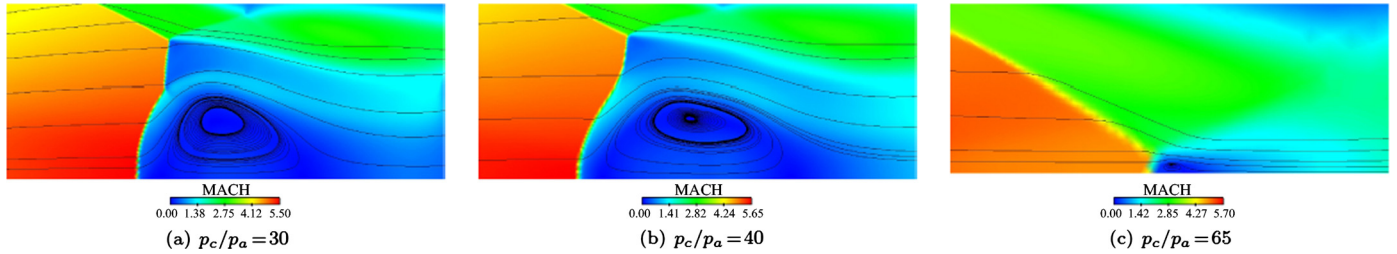(a) $p_c/p_a = 30$ (b) $p_c/p_a = 40$ (c) $p_c/p_a = 65$

Fig. 4. Enlargement of the Mach disc region (Mach number field [min = 0, max = 5.7]).

mesh independent. Results presented thereafter contain approximately 550 000 nodes. Further refinement was not realistic due to excessive computing times.

The computations reported here are performed on a parallel computer (IBM P4 1600) using 20 processors. Using the MPI library, the speed-up is around 90% and the code requires approximately 0.42 ms per iteration and per node on a total number of eight hundred thousand grid points.

The boundary conditions used for this study include inflow, outflow, solid walls with adiabatic conditions and geometrical symmetry. Reservoir conditions (total temperature and total pressure) are fixed as inflow conditions. Two outflow boundary conditions are needed: constant pressure for subsonic flows and extrapolation for supersonic flows. On solid walls, no-slip boundary conditions are specified and axisymmetric conditions are imposed on the centerline of the jet.

3. Results and discussions

The reported numerical Schlieren pictures have been constructed using the density gradient field portrayed on a nonlinear scale in order to expose even weak non-uniformities in the flow density [14].

3.1. Truncated ideal nozzle

The first test-case presented in this paper is an overexpanded sub-scale rocket-nozzle having a Truncated Ideal Contour (TIC), studied experimentally at DLR [34]. The working gas in air and the chamber temperature is $T_c = 300$ K. Ideal nozzles have no internal shock and produce a nearly uniform flow and parallel flow at the exit. The ideal contour can be easily designed with a method of characteristics. Because of the low gradient of the contour at the end, the nozzle can be long enough. However, this low slope inclination shows only negligible contribution to the thrust. Therefore, truncating these nozzles facilitates the use for rocket engines without significant loss in performance due to non-uniformity of the outflow.

For a highly overexpanded regime, i.e. when the exit pressure is much lower than the ambient pressure, a separated flow occurs inside the nozzle and evolves as a free jet. An open recirculation
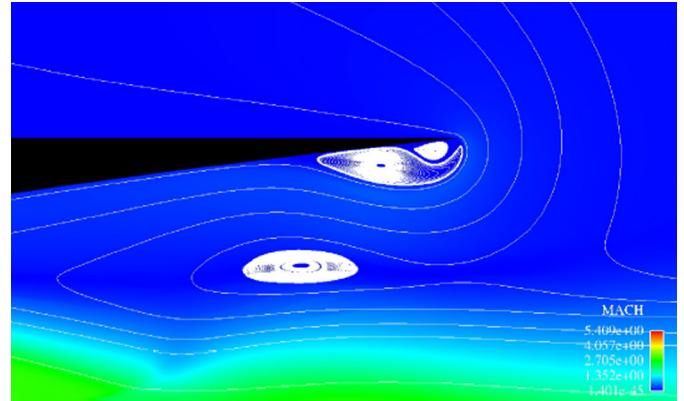

Fig. 5. Trapped vortex at the nozzle lip. Mach number field [min = 0, max = 6.05].

zone exists which matches the ambient free-stream to the supersonic carrier flow.

The computations were carried out using three different Nozzle Pressure Ratios (NPR = P_c/Pa); 30, 40 and 65. A typical flow separation is shown in Figs. 3 and 4. The numerical simulation reveals the existence of a small recirculation bubble trapped between the wall (at the nozzle lip) and the main recirculation zone (see Fig. 5). It has been shown [2] that this small vortex may play an important role in the amplification of the flow oscillations especially at the end-effect regime. As shown by Nguyen [8] (see also Refs. [17,48]), this regime is characterized by very high pressure-fluctuations and occurs at a certain range of pressure ratio when the reattachment line reaches the nozzle lip. In fact, the recirculation bubble induced by the separation shock opens to ambient atmosphere and the flow involves a strong global unsteadiness with very large amplitude fluctuations of about 15–20% of the nozzle divergent length.

The central part of the jet is characterized by a strong shock wave interaction leading to a curved Mach disc structure with a triple point configuration and a downstream recirculation zone (see Fig. 4). This vortex has already been observed in several computations. For instance, Nasuti et al. [24] show that the appearance of this vortex is strongly correlated with the upstream non-uniformities of the flow. This assumption seems to be verified in our calculations, since Fig. 6 clearly shows that the flow upstream
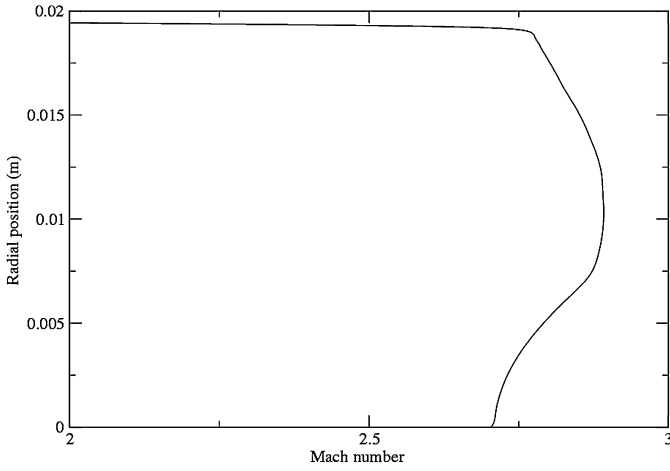
Fig. 6. Radial distribution of the Mach number downstream of the nozzle throat.
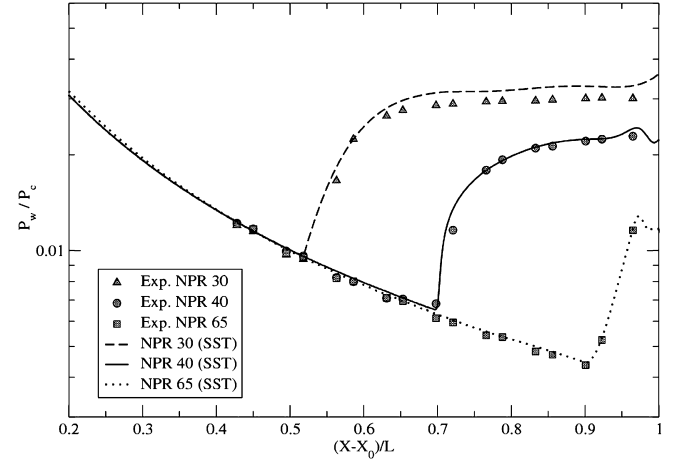

Fig. 7. Normalized wall-pressure distributions for the TIC nozzle at different NPR with $\Theta = 1$.
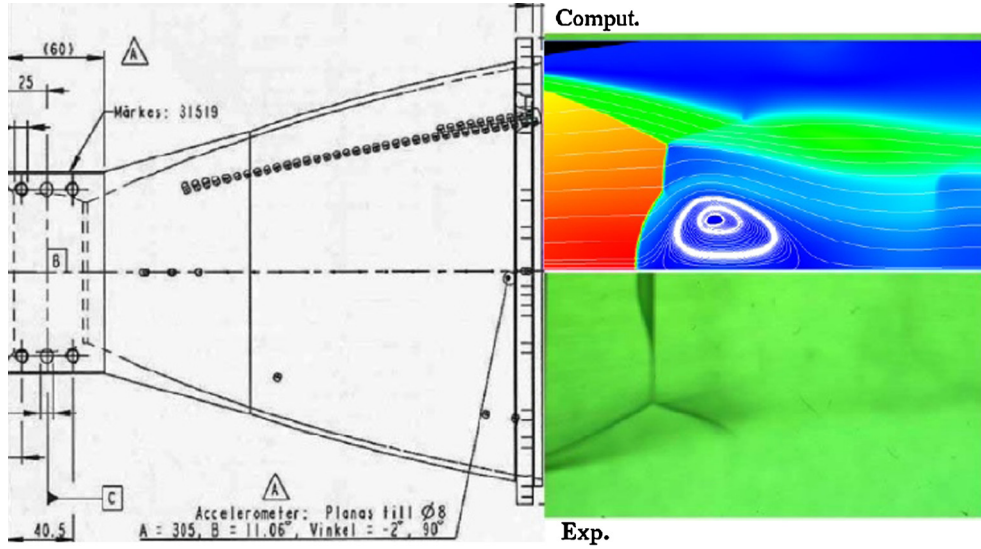

Fig. 8. Flow in a truncated ideal nozzle at NPR = 30. Schlieren photograph from cold-gas test at FOI – Swedish Defence Research Agency [10,42] (bottom) and present numerical simulation showing the Mach field (top).

of the Mach disc is not uniform in the radial direction. The origin of this non-uniformity is directly related to the expansion fan, emanating from the curved shape of the nozzle throat. As expected, for such a nozzle configuration, only a free shock separation structure is observed.

As depicted on Fig. 4, the vortex behind the shock is present for NPR = 20, 30 and 40 but tends to disappear for higher values. In fact, it is theoretically possible to show that a curved shock wave creates a rotational flow downstream. Indeed, a change in thermodynamic quantities through a shock depends crucially on the slope as well as the strength of the shock. Indeed, if the shock is very strong, the velocity downstream of it is very small but positive in all circumstances. However, if after the shock the flow is submitted to a new, but progressive, deceleration imparted by the contiguous field, then a situation can be met where its stagnation pressure becomes less than the local static pressure, so that it is no longer possible for the flow to decelerate with positive velocity.

The corresponding wall pressure distributions are shown in Fig. 7 where the computational results are compared to the experimental data. Excellent agreement is obtained. Furthermore, one-to-one CFD-experiment comparison shows evidence of the Mach disc curvature with convex shape (seen from the inside of the nozzle) in both computation and experiment (see Fig. 8).

3.2. Thrust-optimized nozzle with secondary jet injection

The second test-case concerns an overexpanded sub-scale rocket nozzle with a thrust optimized parabolic (TOP) contour, studied experimentally in the R2Ch wind-tunnel (Onera Meudon-Center) [33]. In this nozzle, an internal shock is shortly induced downstream of the point (at the beginning of the divergent section) where the wall contour undergoes a transition in its curvature from circular arc (which forms the throat section) to parabolic contour. A cap-shock pattern with a trapped vortex results from an interaction of the overexpansion or the separation shock (coming from the nozzle wall) and an inverse Mach reflection of the internal shock at the nozzle centerline [46].

This nozzle is also characterized by the injection of a secondary wall-jet acting as a "film-cooling" at reservoir pressure $p_c = 3.5$ bar and reservoir temperature $T_c = 325$ K. In fact, in rocket nozzles, the secondary flow injection is used to protect the nozzle wall against the hot gases issuing from the combustion chamber and also to increase the specific impulse of the launcher.

In this paper, a parametric analysis was conducted to study the effect of the film cooling on the nozzle flow behavior by changing the Nozzle Pressure Ratio (NPR) as well as the total tem-
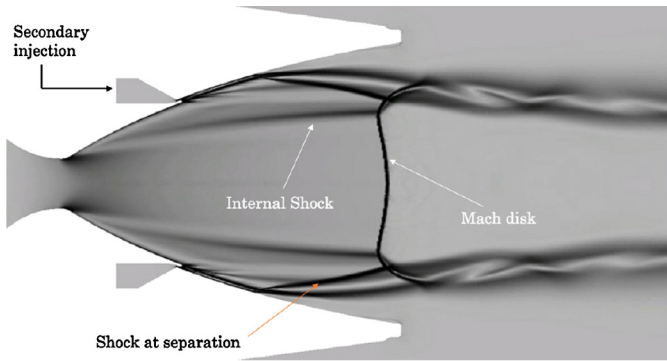
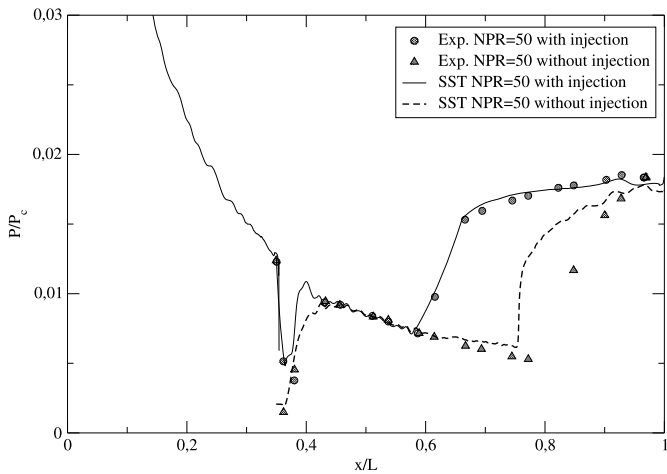**Fig. 9.** Numerical Schlieren picture of the TOP nozzle with a film injection at $NPR = 50$.

Fig. 10. Normalized wall–pressure distributions for the TOC nozzle at $NPR = 50$.

Fig. 11. Normalized wall–pressure distributions for the TOC nozzle at $NPR = 30$.

perature ratio between the main flow and the secondary flow, $\Theta = T_{c,mf}/T_{c,film}$.

Fig. 9 depicts the Mach-number field for a pressure ratio of 50. The computations show a free shock separation with the formation of a highly compressible mixing layer surrounding the overexpanded supersonic jet. In the central part of the nozzle, an inverse Mach reflection of the internal shock occurs (with a slightly curved Mach disc shape) which interacts with the overexpansion shock to form a cap-shock pattern. As depicted in Fig. 10, the SST model in the case of nozzle with film cooling correctly predicts the distribution of the nozzle wall pressure. The first pressure jump corresponds to compression waves, located in the injection zone (step), while the second jump is due to the boundary layer separation. However, in the absence of the film, the separation point is slightly shifted upstream compared to the experimental data. This difference is probably due to the way the interaction area of secondary injection was modeled. Indeed to simulate the case without film injection, the secondary-nozzle exit was closed by an artificial flat and was modeled as a wall. This is observed to result in a recirculating flow similar to that formed downstream of a backward facing step. However, in the experiment, the nozzle was blocked far downstream of the throat, which forms a subsonic cavity with a large area of stagnant flow. Obviously, the two flows are not identical and it is likely that the point of separation will be affected. Moreover, one can notice that when the pressure ratio increases, the separation point, as well as the Mach disc, moves downstream (see Figs. 10 and 11).

Figs. 12 and 13 show the Mach-number fields in cold gas for $NPR = 30$ and 50 with and without film injection. The first remark, which holds true for both pressure ratios, is that the com-
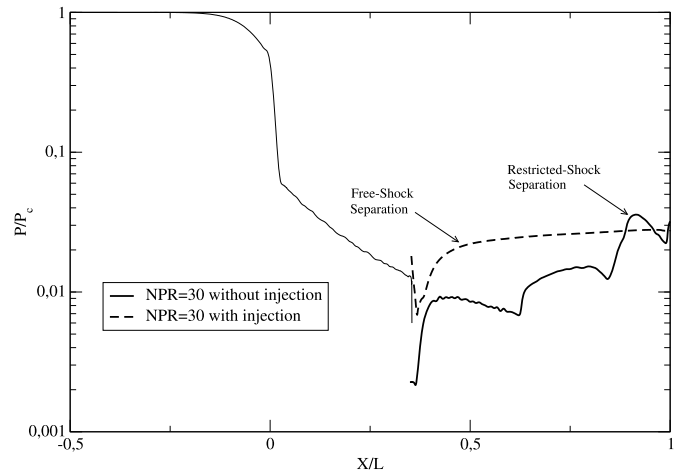
putation without film cooling shows a central re-circulation zone the extent of which more or less depends on the Mach disc location. This cap-shock structure is a well-known characteristic of the thrust-optimized nozzles. Moreover, in the presence of film injection for similar pressure ratio, the separation point is located upstream. This can be explained by the fact that the boundary-layer, downstream of the location of secondary injection, is less energetic compared to that in the main stream as the chamber pressure of the secondary flow is less. As a result, the boundary-layer separates much earlier. On the other hand, it can be noticed that depending on the chamber conditions and the presence or absence of secondary injection, the flow topology is completely different.

It can be seen that although a cap-shock pattern is present in all the simulations involving a film injection, none of the computational results showed RSS condition but only FSS condition (see Fig. 9). Thus, it is evident that the film plays an important role on the operating nozzle flow regime, since no RSS configuration has been observed despite the existence a cap-shock pattern and an internal shock. This result can be partially explained by using the model of Frey and Hagemann [9]. As previously mentioned, the reattachment of the boundary layer is mainly due to the presence of a cap-shock pattern. In fact, crossing the separation shock, the flow is deflected towards the axis of symmetry. On the other hand, the oblique shocks emanating from the cap-shock configuration deflect the flow towards the wall, which promotes the reattachment of the jet. Thus, if the deviation of the flow generated by the recompression shock prevails over that induced by the oblique shock (case of nozzle with secondary injection) the free shock separation appears. If, however, the second deviation is larger (case of nozzle with no injection) the jet will reattach to the wall. In other terms, based on a momentum balance across the cap-shock pattern, the model of Frey and Hagemann [9] allows to evaluate the relative importance of these two contributions and to deduce the type of separation, i.e. free or restricted shock separation. Based on these results, it is clear that the secondary injection promotes the free shock separation regime. A similar observation is recently reported by Verma and Haidn [47] while testing a TOP nozzle in a high altitude simulation chamber (HASC). For similar NPR inside the HASC, the separation location shifts upstream relative to sea-level testing. As a result no RSS was observed at any operating condition.

In the vicinity of the secondary nozzle, the numerical simulation shows the structure of the mixing layer formed between the two co-flowing streams. The incident recompression shock, emanating from the leading edge of the entrainment zone, impinges
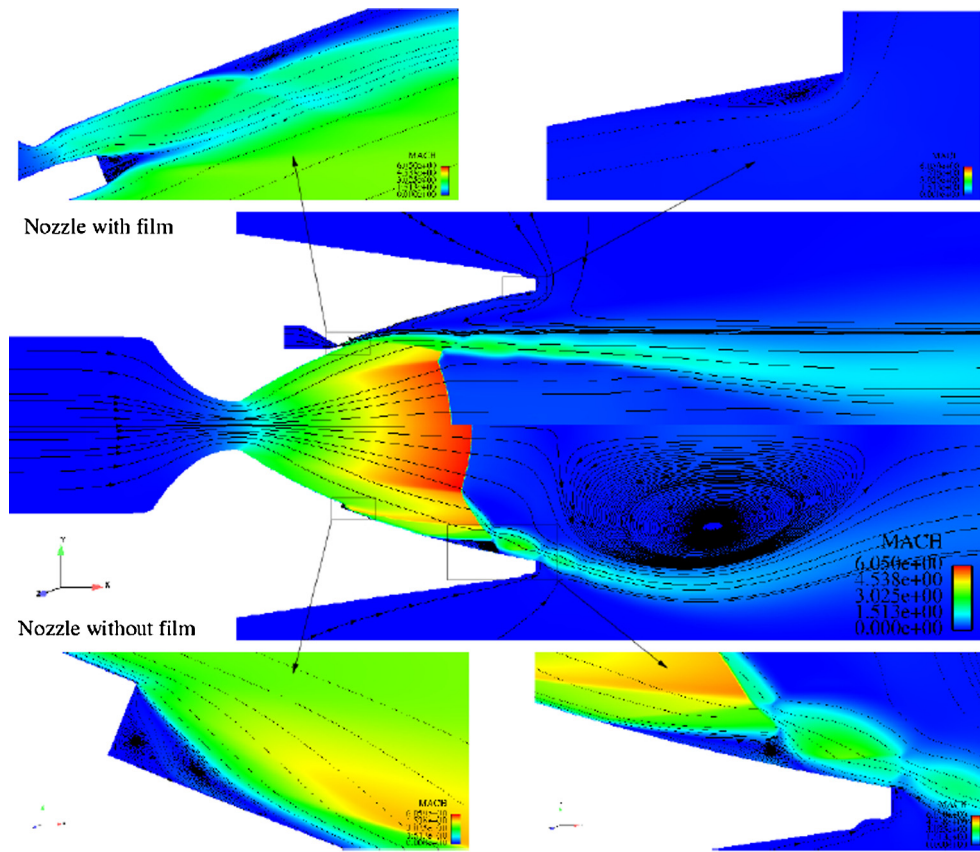
Fig. 12. Mach number distribution with streamline contours for NPR = 30 with (top) and without (bottom) film injection [min = 0, max = 6.05].
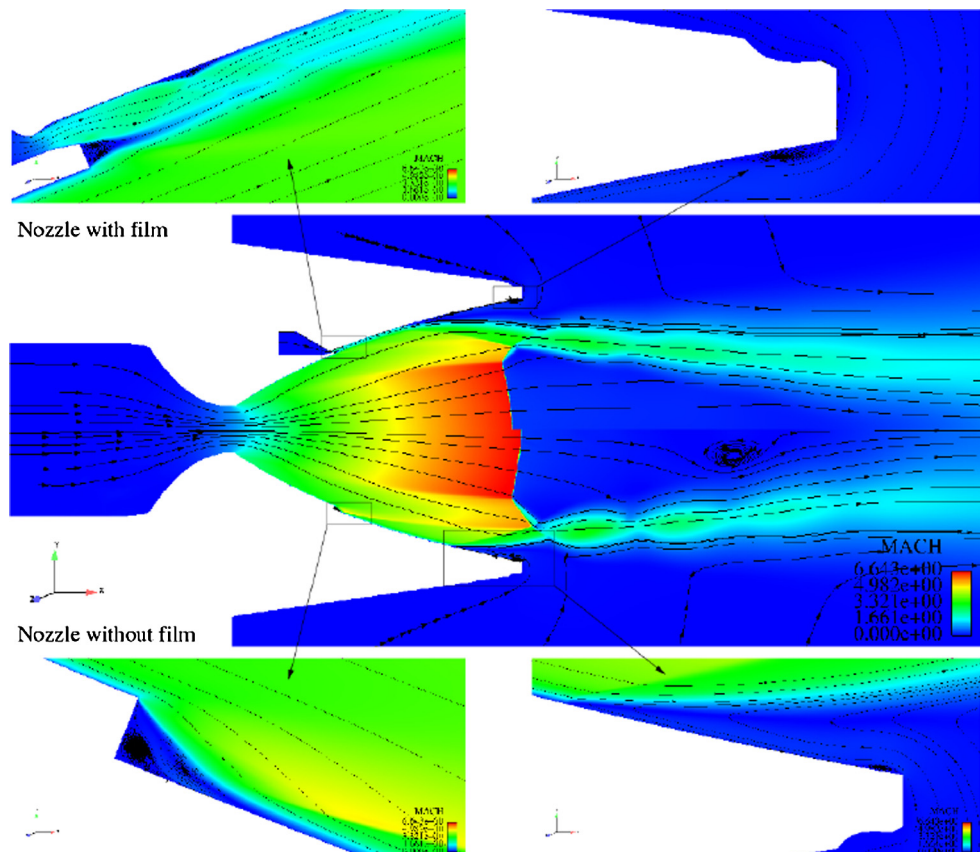

Fig. 13. Mach number distribution with streamline contours for NPR = 50 with (top) and without (bottom) film injection [min = 0, max = 6.05].
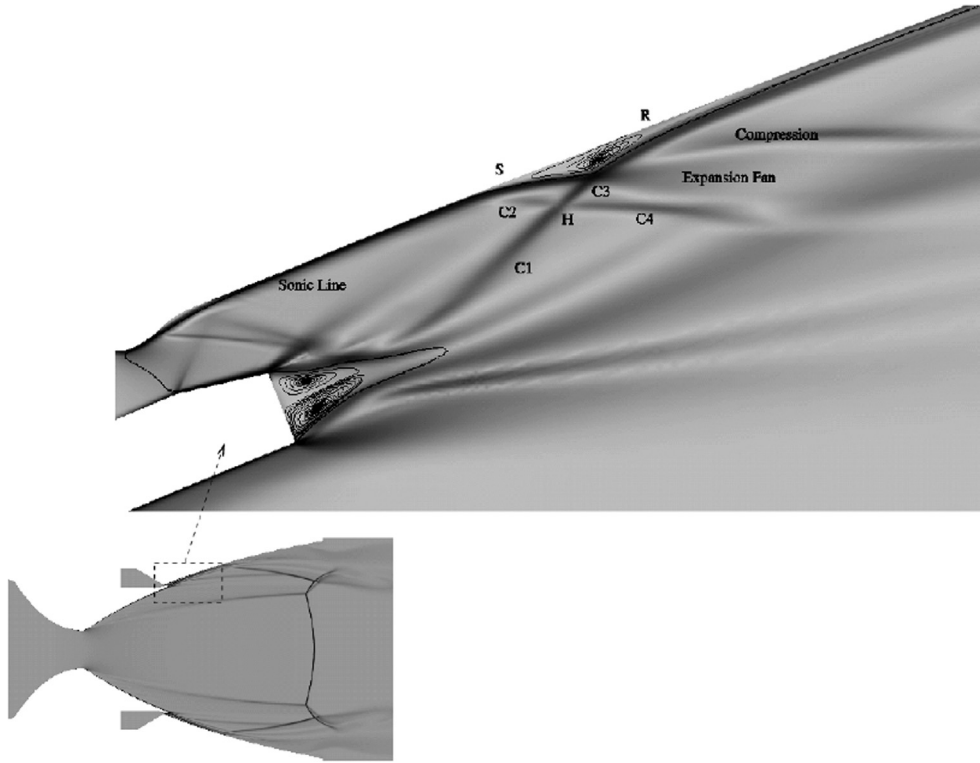
Fig. 14. Numerical Schlieren picture at NPR = 50 with enlargement of the near-wall injection region.
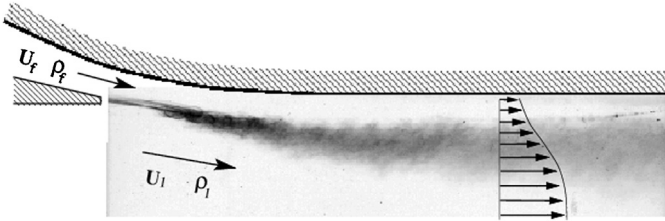

Fig. 15. Secondary jet injection with the formation of wall-mixing layer.

on the boundary layer, and provokes its separation (see Fig. 14). It is important to notice that when the distribution of the total pressure in the secondary nozzle is not homogeneous, the flow in the reinjection area is affected, which may induce strong side loads. Indeed, since the shock/boundary layer interaction induces a strong increase of pressure with possible flow asymmetry, the corresponding load can be particularly significant [41].

A numerical Schlieren picture of the flow-field (Fig. 14) highlights the major features occurring in this nozzle. The boundary layer separates at point S, located upstream of the incident shock. The rapid pressure jump at separation occurs as a result of the compression waves. These waves coalesce to constitute the leading reflected shock C2 through which the outer stream is turned upward from the wall. The shock C2 intersects the incident shock C1 at point H where two reflected shocks C3 and C4 are formed. After its intersection with the C2, the shock C1 is curved because of the entropy jump downstream of C2 and the compression waves generated by the thickening of the boundary layer. Thus the impingement of C1 on the boundary layer can be similar to a shock reflection at a constant pressure free-boundary, as is the case of the outer boundary of a larger separated region. The flow reattaches downstream (point R) leading to a formation of a recirculation zone with a strong increase in the thickness of the boundary layer. Downstream of the interaction zone, the flow relaxes and recovers a usual behavior.
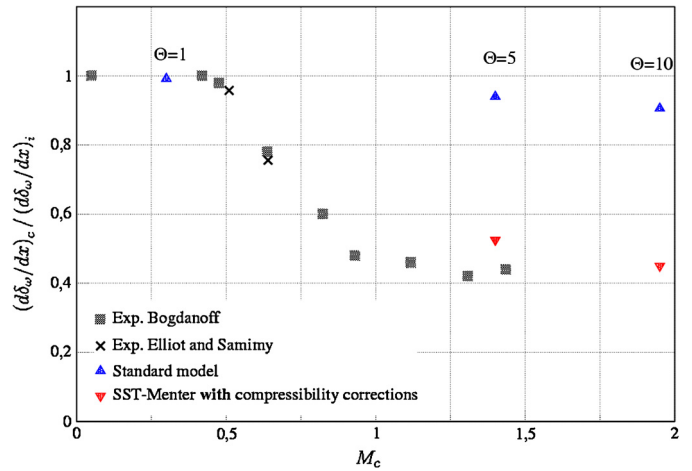

Fig. 16. Compressibility effect on normalized vorticity thickness of the near-wall mixing-layer growth rate. $(d\delta_\omega/dx)_i = \frac{1}{11}(1-r)(1+\sqrt{s})/(1+r\sqrt{s})$ with r and s are ratios of velocities and densities, respectively, and $(d\delta_\omega/dx)_c = \frac{\Delta U}{|\partial U/\partial y|_{max}}$, with $\Delta U = U_1 - U_f$. The convective Mach number M_c is defined as [4]: $M_c = (U_1 - U_f)/c$, where U_1 is the main flow velocity, U_f is the film cooling velocity and c is the mean speed of sound.

Moreover, we have investigated the compressibility effects in the mixing layer formed between the two streams at the base of the injection (see Fig. 15). It is well known that, for compressible flows, the mixing growth rate decreases when the convective Mach number increases [30]. In the present case, when the temperature ratio increases, the convective Mach number increases and the compressibility effects become significant. Fig. 16 shows the influence of the gas effects on the behavior of the mixing layer. When the pressure dilatation terms, $\overline{p''d''}$, are neglected the computation fails to correctly reproduce the spreading rate of the mixing layer, whereas results including compressibility effects provide a better prediction. Apart from the convective Mach number,
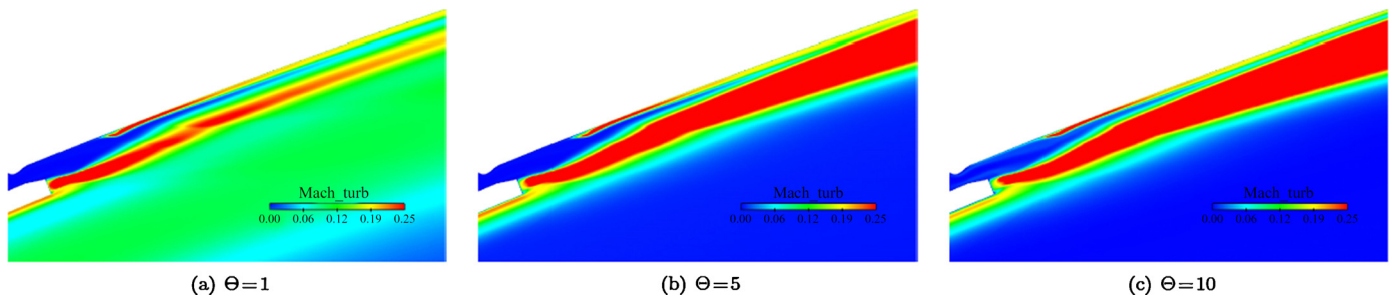
(a) $\Theta=1$ (b) $\Theta=5$ (c) $\Theta=10$

Fig. 17. Turbulent Mach number field, $M_t = \frac{\sqrt{2k}}{c}$ [min = 0, max = 0.25].

there are other relevant Mach numbers with including the turbulent Mach number, M_t. Fig. 17 shows the spatial evolution of the turbulent Mach number, M_t, which one of the parameter used to measure the importance of the compressibility effects on the mixing layer.

The results indicate how the main flow and the film cooling interact for different temperature ratios. The thickness growth rate of the shear layer formed by the two supersonic streams exhibits a large reduction with the increasing values of M_t.

4. Conclusions

In this study, the SST-Menter turbulence model with compressibility effects has been used to investigate shock-induced boundary-layer separation in supersonic overexpanded nozzles with and without secondary jet injection. In order to improve the robustness of the numerical code, specific treatments of the turbulent quantities have been introduced to avoid numerical oscillations during transient solutions [32]. The obtained results of the TIC nozzle show a good prediction of the separation point and reveal the effects of upstream non-uniformities of the nozzle flow on the Mach disc curvature and related vortex generation. The computation of the TOP nozzle highlights the complexity of the flow structure downstream of the secondary nozzle. In particular, the existence of shock wave/boundary-layer interaction with the re-circulation bubble downstream of the injection location is shown. Wall-jet injection is observed to initiate early separation in a TOP nozzle which significantly modifies the momentum imbalance across the overexpansion and reflected shocks in the cap-shock pattern. This prevents RSS condition to occur at all operating conditions and can have significant implications from the viewpoint of side-load generation. In addition, this study shows that the compressibility effects within the mixing layer, formed between the main jet and the secondary injection, are important and cannot be neglected in the computation. Indeed, in hot gases the thickness of the mixing layer is reduced in comparison with cold gas, which induces a delay in the entrainment of the film cooling by the main flow. Further investigations should consider the real gas effects with heat release and combustion. The objective is to develop reliable CFD tools for the prediction of the aerothermodynamics phenomena in supersonic nozzles with possible coupling between fluid, structure and heat transfer.

Conflict of interest statement

No conflict of interest.

Acknowledgements

References

[1] K. Abdol-Hamid, S. Pao, C. Hunter, K. Deere, S. Massey, A. Elmiligui, PAB3D: its history in the use of turbulence models in the simulation of jet and nozzle flows, AIAA Paper 06-489, 2006.

[2] T. Alziary de Roquefort, Unsteadiness and side-loads in over-expanded supersonic nozzles, in: Proc. of the 4th European Symposium on Aerothermodynamics for Space Vehicles, Capua, Italy, 15–18 October, 2001.

[3] H. Amann, Experimental study of the starting process in a reflection nozzle, Phys. Fluids Suppl. 12 (1967) 150–153.

[4] D.W. Bogdanoff, Compressibility effects in turbulent shear layers, AIAA J. 21 (1983) 926–927.

[5] R. Carpentier, Approximation et analyse numérique d'écoulements instationnaires, application à des instabilités tourbillonnaires, Ph.D. thesis, University of Nice, France, 1995.

[6] C. Chen, S. Chakravarthy, C. Hung, Numerical investigation of separated nozzle flows, AIAA J. 32 (1994) 1836–1843.

[7] S. Deck, A. Nguyen, Unsteady side loads in a thrust-optimized contour nozzle at hysteresis regime, AIAA J. 42 (2002) 1878–1888.

[8] W.A. Engblom, A. Khavaran, J. Bridges, Numerical prediction of chevron nozzle noise reduction using WIND-MGBK methodology, AIAA Paper 04-2979, 2004.

[9] M. Frey, G. Hagemann, Flow separation and side-loads in rocket nozzles, AIAA Paper 99-2815, 1999.

[10] M. Frey, A. Preuss, G. Hagemann, S. Girard, T. Alziary, P. Reijasse, R. Stark, K. Hannemann, R. Schwane, D. Perigo, L. Boccaletto, H. Lambaré, Joint European effort towards advanced rocket thrust chamber technology, in: The 6th International Symposium on Launcher Technologies, Munchen, Germany, 8–11 November 2005.

[11] N. Georgiadis, C. Rumsey, D. Yoder, K. Zaman, Turbulence modeling effects on calculation of lobed nozzle flowfields, J. Propuls. Power 22 (2006) 567–575.

[12] A. Gross, C. Weiland, Investigation of shock patterns and separation behaviour of several subscales nozzles, AIAA Paper 2000-3293, 2000.

[13] A. Gross, C. Weiland, Numerical simulation of separated cold gas nozzle flows, J. Propuls. Power 20 (2004) 509–519.

[14] A. Hadjadj, A. Kudryavtsev, Computation and flow visualization in high-speed aerodynamics, J. Turbul. 21 (2005) 1–25.

[15] A. Hadjadj, A. Kudryavtsev, M. Ivanov, Numerical investigation of shock-reflection phenomenon in overexpanded supersonic jets, AIAA J. 42 (3) (2004) 570–577.

[16] A. Hadjadj, M. Onofri, Nozzle flow separation, Shock Waves 19 (2009) 163–169.

[17] G. Hagemann, M. Frey, W. Koschel, Appearance of restricted shock separation in rocket nozzles, J. Propuls. Power 18 (2002) 577–584.

[18] D. Kenzakowski, Turbulence model improvements for jet noise prediction using PIV datasets, AIAA Paper 04-2978, 2004.

[19] D. Knight, G. Degrez, Shock wave boundary layer interactions in high Mach number flows – a critical survey of current CFD prediction capabilities, AGARD AR-319, 2, 1998.

[20] B. Lakshmanan, K. Abdol-Hamid, Investigation of supersonic jet plumes using an improved two-equation turbulence model, J. Propuls. Power 10 (5) (1994) 736–741.

[21] R. Lawrence, Symmetrical and unsymmetrical flow separation in supersonic nozzles, Research report 67-1, Southern Methodist University, April 1967.

[22] F. Menter, Zonal two equation k–ω turbulence models for aerodynamic flows, AIAA Paper 93-2906, 1993.

[23] J. Moore, J. Moore, Realizability in two-equation turbulence models, AIAA Paper 99-3779, 1996.

[24] F. Nasuti, M. Onofri, Shock structure in separated nozzle flows, Shock Waves 19 (2009) 229–237.

[25] L. Nave, G. Coffey, Sea-level side loads in high-area-ratio rocket engines, AIAA Paper 73-1284, 1973.

[26] A. Nguyen, H. Deniau, S. Girard, T.A. de Requefort, Unsteadiness of flow separation and end-effects regime in a thrust-optimized contour rocket nozzle, Flow Turbul. Combust. 71 (2003) 1–21.

[27] J. Ostlund, Flow processes in rocket engine nozzles with focus on flow-separation and side-loads, Ph.D. thesis, TRITA-MEK, Royal Inst. of Tech., Stockholm, 2002.

[28] J. Ostlund, T. Damgaard, M. Frey, Side-loads phenomena in highly over-expanded rocket nozzles, J. Propuls. Power 20 (2004) 695–704.

[29] S. Pao, K. Abdol-Hamid, R. Campbell, C. Hunter, S. Massey, A. Elmiligui, Unstructured CFD and noise prediction methods for propulsion airframe aeroacoustics, AIAA Paper 06-2597, 2006.

[30] D. Papamoschou, A. Roshko, The compressible turbulent shear layer: an experimental study, J. Fluid Mech. 197 (1988) 453–477.

[31] S. Park, J. Kwon, Implementation of k–ω turbulence models in an implicit multigrid method, AIAA J. 42 (7) (2004) 1348–1357.

[32] Y. Perrot, A. Hadjadj, Numerical simulation of shock/boundary layer interaction in supersonic nozzles, AIAA Paper 05-4309, 2005.

[33] P. Reijasse, Description of nozzle test cases, ATAC Nozzle Workshop DAFE/D-20/02, 2002.

[34] P. Reijasse, L. Morzenski, D. Blacodon, J. Birkemeyer, Flow separation experimental analysis in overexpanded subscale rocket-nozzles, in: 37th AIAA/ASME/SEA/ASEE Joint Propulsion Conference and Exhibit, 2001, AIAA-Paper 2001-3556.

[35] P. Roe, Approximation Riemann solvers, parameters vectors and difference schemes, J. Comput. Phys. 43 (1981) 357–372.

[36] S. Sarkar, Modeling the pressure–dilatation correlation, Progress report, NASA Langley Research Center, Inst. for. Computer Applications in Science and Engineering, May 1991.

[37] S. Sarkar, G. Erlebacher, M. Hussaini, Compressible homogeneous shear: simulation and modeling, in: Turbulent Shear Flows, Springer-Verlag, 1992, pp. 247–267.

[38] SIMULOG, N3S-Natur V1.4, logiciel 3D Navier–Stokes, Logiciel, manuels théorique, utilisateur et informatique, 2001.

[39] R. Stark, W. Kwan, F. Quessard, G. Hagemann, M. Terhardt, Rocket nozzle cold gas test campaigns for plume investigations, in: The 4th European Symposium on Aerothermodynamics for Space Vehicles, Capua, Italy, 2001.

[40] T. Tomita, H. Sakamoto, T. Onodera, M. Sasaki, M. Takahashi, H. Tamura, Y. Watanabe, Experimental evaluation of side-loads characteristics on TP, CTP and TO nozzles, AIAA Paper 04-3678, 2004.

[41] T. Tomita, M. Takahashi, M. Sasaki, H. Sakamoto, M. Takahashi, H. Tamura, Experimental evaluation of side-loads in LE-7A prototype engine nozzle, Shock Waves 19 (2009) 213–228.

[42] L. Torngren, Correlation between outer flow and internal nozzle pressure fluctuations, in: The 4th European Symposium on Aerothermodynamics for Space Vehicles, Capua, Italy, 2001.

[43] B. van Leer, Towards the utlimate conservative difference scheme: the quest of monotonicity, in: Lecture Notes in Physics, vol. 18, 1972, p. 163.

[44] S. Verma, Study of flow separation in truncated ideal contour nozzle, J. Propuls. Power 18 (2002) 1112–1121.

[45] S. Verma, Shock unsteadiness in a thrust optimized parabolic nozzle, Shock Waves 19 (2009) 193–212.

[46] S. Verma, O. Haidn, Study on restricted shock separation phenomena in a thrust optimized parabolic (TOP) nozzle, J. Propuls. Power 25 (2009) 1046–1057.

[47] S. Verma, O. Haidn, Flow separation characteristics of a thrust optimized parabolic nozzle in a high altitude simulation chamber, in: 46th AIAA Joint Propulsion Conference, Nashville, 25–28 July 2010.

[48] Q. Xio, H. Tsai, D. Papamoschou, Numerical investigation of supersonic nozzle flow separation, AIAA J. 45 (2007) 532–541.

[49] O. Zeman, Dilatational dissipation: the concept and application in modeling compressible mixing layers, Phys. Fluids 2 (2) (1990) 178–188.